

Focused-Ion-Beam for chiral photonics

Subjects: Nanoscience & Nanotechnology

Contributor: Mariachiara Manoccio

Focused ion beam (FIB) processing which enabled scientific and technological advances in the realization and study of micro- and nano-systems in many research areas, such as nanotechnology, material science, and the microelectronic industry. Recently, its applications have been extended to the photonics field, owing to the possibility of developing systems with complex shapes, including 3D chiral shapes. Micro-/nano-structured elements with precise geometrical features at the nanoscale can be realized by FIB processing, with sizes that can be tailored in order to tune optical responses over a broad spectral region. In this entry, we give an overview of the recent efforts in this field which have involved FIB processing as a nanofabrication tool for photonics applications. In particular, we focus on FIB-induced deposition and FIB milling, employed to build 3D nanostructures and metasurfaces exhibiting intrinsic chirality.

Keywords: focused ion beam milling ; focused ion beam induced deposition ; 3D nanostructuring ; chirality ; chiral photonics ; circular polarization ; chiroptical effects

1. Introduction

The development of systems of increasing complexity, enabled by the advanced nanofabrication technologies which are available today, is increasing the potential of nanophotonics ^[1]. Metamaterials and photonic crystals with accurate and tunable geometries at the nanoscale level can now be manufactured, broadening the scope of possibilities from traditional planar geometries to complex systems, and making it possible to explore new optical properties and to modulate light-matter interactions in specific spectral regions ^{[2][3][4]}.

One example is represented by chiral optical systems. Chirality is a geometric feature which is characterized by a lack of specular symmetry. It is present in many forms in nature, such as molecules, proteins, our hands, and even galaxies ^[5]. This geometric feature is of great importance in the study of chemistry and biology because two enantiomers (i.e., two specular images of each other) may have different physiological responses, even though they do not seem to differ in terms of their chemical and (almost all) physical properties. As an example, one enantiomer can provoke toxic pharmacological effects while another is innocuous ^[6]. However, the only way to distinguish between the two turns out to be the interaction of the molecules with circularly polarized light (CPL). Thus, study of the optical responses of these systems is very important, because it allows researchers to distinguish between two apparently identical enantiomeric forms. However, chiro-optical effects are very faint in molecules because of their small dipole moments, and they are generally observed only in the ultraviolet (UV) region. Artificial chiral photonic structures with nanoscale dimensions, mimicking natural chiral molecules, can be engineered in such a way that these effects are boosted, making them observable also in the VIS and IR range ^[7]. These structures have been applied in a broad range of investigation fields, from the sensing of biomolecules to miniaturized and integrated devices ^[8], as we will see in the following paragraphs. Chiral metamaterials ^{[9][10]} and chiral plasmonic nanostructures ^{[11][12]} exhibit extraordinary optical properties ^{[13][14]} which are strongly enhanced when they are designed in three dimensions, where geometrical chirality is more pronounced ^[15]. However, the fabrication of 3D nanostructures with intrinsic chirality is very challenging, because complex shapes such as spirals ^[7] must be realized with a high level of accuracy and spatial resolution to ensure reliability and reproducibility in optical experiments ^[16]. New strategies to fabricate complex 3D chiral objects at the micro- and nano-scales are nowadays in great demand. Focused ion/electron beam technology has demonstrated the ability to manipulate materials at the nanometer scale by directly patterning the substrate to create nanostructures with a high degree of precision ^[17] and without limitations in terms of structural complexity, making it possible to include 3D and chiral features. Compared to other nanofabrication techniques, focused ion/electron beam technology stands out for many reasons, such as its enormous flexibility in 3D design, but also because it requires only a single technological step, is compatible with many materials, and requires little preparation time ^[18]. Focused ion beam (FIB) technology found its first applications in the semiconductor industry ^[19], in the repair of defects in lithography photomasks ^{[20][21]}, in circuit modifications ^[22], in transmission electron microscope (TEM) sample preparation ^{[23][24]}, and in failure analyses ^[25]. Subsequently, FIB processing has been used for the fabrication of tools for atomic force microscopy (AFM) ^[26] and scanning optical near-

field (SNOM) microscopy [27]. Nowadays, its fields of application have been extended to include various research areas requiring nanometer-scale imaging, lithography, material removal, and deposition. The recent progress of this technology has allowed entry into the nanophotonic field of research [28], which was not accessible before, mainly because of limited control of the process yield at the nanoscale, along with fundamental issues related to material composition.

2. Focused Ion Beam Processing

In recent years, FIB processing has gained much interest for the creation of prototypes of three-dimensional nanostructures for applications in photonics, thanks to its very high spatial resolution and flexibility regarding structural design. With FIB processing, the fabrication of complex nanostructure, can occur through material removal caused by the ion milling capability, or through local deposition induced by the interaction between the ion beam and a gaseous precursor.

Remarkably, this technology can work with both material families of interest for nanophotonics, i.e., conductive and lossy metals, and insulating and low losses dielectrics. FIB processing is usually carried out in a vacuum chamber, equipped with both electron and ion optical columns even though, in this review, we are focusing on the ion beam-processing. The high energy beam is emitted from an ion source, accelerated at energies ranging from 5–50 KeV, and focused on the sample surface by means of a series of electrostatic lenses. By adjusting the current passing through the lens, the beam can be finely focused, achieving a spot size as narrow as 10 nm [29].

When the ion beam interacts with the sample surface, many phenomena occur [30]:

- Emission of secondary electrons, usually employed for sample imaging;
- sputtering of the substrate atoms;
- deposition in the presence of gaseous precursors in the chamber; and
- re-deposition of some sputtered atoms and ion implantation from the beam, leading to amorphous/damaged/rough surfaces.

The design and manufacturing of the nanostructures with focused ion beams is ruled by several parameters which define the resolution, the pattern dimension (pixels), and the quality of the structures. These parameters are: the ion species, the ion dose, the incident angle, the beam energy, and the accelerating voltage. The nanofabrication is also driven by pattern parameters, such as the dwell time (i.e., the time during which the ion beam stays in one position), and the step size (i.e., the distance between two consecutive beam positions).

Moreover, the patterning of complex geometries at micro- and nano-scale takes advantage of computer-aided design and manufacturing systems, particularly helpful in improving dimensional accuracy and reproducibility during fabrication [31].

The focused ion beam (either with heavy ions like Ga⁺ [32], or light ions like He⁺ [33]) can be also employed as a scanning ion probe for lithographic patterning in resists, with position and timing controlled by a pattern generator. The ion beam lithography reaches higher resolution as compared to EBL, even if with the same spot size, thanks to the absence of backscattering effects together with a weaker forward scattering and a smaller lateral diffusion of secondary electrons [34]. Moreover, the ions, heavier than electrons, can penetrate the sample with higher energy, allowing a faster exposure of the resists and a faster processing [34][35] of photonics nanostructures.

2.1. Basics of FIB Milling

A scheme of the FIB milling process is reported in [Figure 1a](#). During the process, which is highly destructive for the sample, the ion beam locally scans the surface digging the targeted area. The milling of the surface can be integrated with gas-assisted etching if gaseous organic precursors are simultaneously introduced in the vacuum chamber through a gas injection system (GIS) [36].

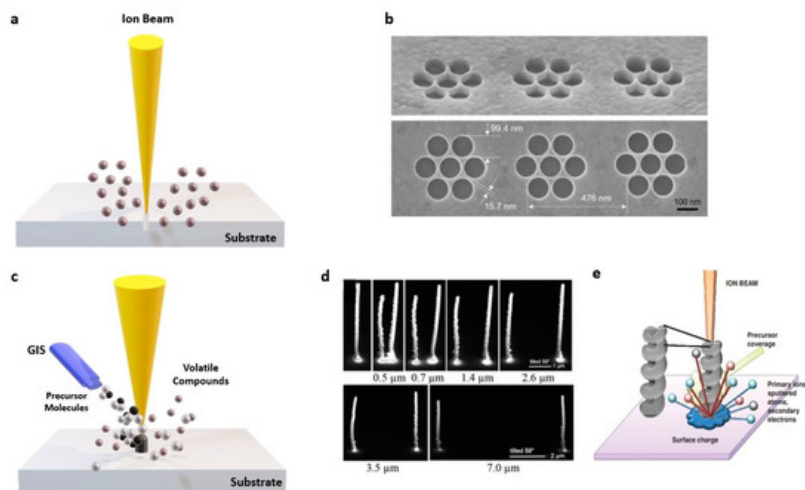


Figure 1. (a) Scheme of the focused ion beam milling. The ions coming from the beam collide on the surface, digging the targeted area. (b) Helium Ion Microscope (HIM) images of 54° tilted view (top) and top view (bottom) of plasmonic nanohole arrays realized with He⁺ milling on Au/SiO₂ substrate. The array consists of seven close-packed holes with 100nm diameter and separated by 15nm of sharp edges without milled material redeposition. Reproduced with permission from [37]. (c) Scheme of the focused ion beam induced deposition (FIBID) procedure: The ions coming from the beam decompose the precursor molecules coming from the gas injection systems leaving a deposit on the substrate. The residual organic compounds are removed from the vacuum system. (d) Scanning electron microscope (SEM) images representing the proximity effect for six pillar pairs with different separations gaps from 0.5 up to 7.0 μm. The metal-organic precursor gas (CH₃)₃Pt(CpCH₃) is used as the gas source. The pillars have been grown on a Si₃N₄/Si wafer. Reproduced with permission from [38]. (e) Schematic image representing all the effects happening during the FIBID process in the fabrication of a multiple loops nanohelix: The interaction with the sample led to scattered particles, charge effects, and proximity effects. Reproduced with permission from [39].

In the milling process, the sputtering rate is ruled by the energy of the beam, which hits and locally removes the substrate atoms. During the sputtering removal, the ions are implanted into the sample.

The most used source is the gallium liquid metal ion source (LMIS) [40]. Alternative and less common LMIS based on other metals, such as B, Be, Si, Sn, Au, Fe, Ni, Cr [41], and alloys like PdAs, PdAsB, AuSi, and AuSiBe, have been also developed and are currently studied [42][43].

The liquid metal lies in contact with a tungsten tip. When applying a high voltage, the heated metal wets the tungsten tip, generating a strong electric field on the tip, which leads to the ionization and the emission of the gallium beam. Ga⁺ LMIS is considered the most advantageous solution because of its low melting point (303 K) and low vapor pressure [41]. A focused Ga⁺ beam can hit the sample with current ranging from 1 pA to 10 nA, with minimum spot size smaller than tens of nanometer [44][45]. However, the sputtered gallium ions cause significant material redeposition and ion implantation on the substrate. To avoid surface damaging and ion implantations, the gas field ionization sources (GFIS) can be employed [46]. These sources are based on the ionizations of helium or neon, which have smaller atomic sizes than gallium. GFIS have been optimized for fabricating nanostructures with very small geometric features, such as nanopores and nanoribbons [47][48].

A He⁺ FIB system provides very small milling currents (0.1 nA) and an ultra-narrow beam spot of less than 0.5 nm [49] with milling resolution of 3.5 nm [50]. The direct He⁺ FIB milling of an Au film was able to produce high-quality nanostructures, such as plasmonic systems consisting of seven close-packed holes, with a 100 nm diameter and very sharp edges, separated from each other by only 15 nm, [37] as shown in Figure 1b. Moreover, in this case, a limited effect of material redeposition from the substrate has been observed.

Other types of sources, largely employed in plasma-based FIB microscopes, are noble gases of heavy ion species, such as Xe or Ar. They can deliver high current beams up to microampere and, because of their larger size, they can be employed for the fast milling of large volumes (up to hundreds of cubic micron) [51].

Since the ion beam is highly localized, it allows for the integration of plasmonic nanostructures on small structures, such as the tips of optical fibers, inducing light-manipulation capabilities as plasmon waveguides [52]. Recently, this concept has been extended also to metasurfaces integrated on optical fibers, for the promising perspectives of optical metasurface sensors on fiber [53].

2.2. Basics of FIBID Growth Dynamics

The first approaches of controlled focused ion/electron beam induced deposition (FIBID/FEBID) growth were investigated in [17][36][54][55], paving the way to the micro/nanofabrication of precise and complex-shaped 3D structures. Today, the availability of different gas precursors [36] to be used in conjunction with the beam is enabling a wide gamut of optical, magnetic, superconducting, and mechanical properties [54][39][56][57].

FIBID procedure works on the principle of local chemical vapor deposition (CVD) [44]. The ion beam breaks the gas precursor molecules coming from the GIS, and leaves a deposit on the substrate, acting as a nucleation site for the nanostructure growth, as schematically illustrated in [Figure 1c](#). Once the design and the proper growth parameters are defined, the precursor decomposition occurs in the targeted area irradiated by the beam, following the beam pattern. The evolution in the third dimension occurs when the beam reaches the edge of the fabricating structure. The secondary electrons emitted during the process enhance the lateral growth on the sample [30][58].

There are many physical mechanisms generated by the interplay with the beam and the substrate which influence the growth in the third dimension. These include secondary electrons emission, scattered particles, and charge effects. In the case of the consecutive growth of several elements, proximity effects are generated due to the bending of the electrostatic force between two neighboring structures. It has been shown that during the growth of two consecutive metallic pillars, the second pillar becomes taller than the first one, while the first pillar becomes broader and slightly folds toward the second one. The studies on proximity effects of Pt-based pillars grown on a $\text{Si}_3\text{N}_4/\text{Si}$ wafer [38] have shown that the scattered ions and the emitted secondary electrons and atoms produced during the second pillar growth induce additional deposits for the first pillar, which, in turn, broadens its diameter. Consequently, the amount of the deposited material induced by proximity effects varies with the separation gap, as shown in [Figure 1d](#). However, for more complex nanostructures like 3D chiral nano helices [39], proximity effects also occur during the growth of the single structure, because of a larger interaction volume of the spiral with the radially scattered particles (schematic illustration of [Figure 1e](#)), as compared to the nanopillar case. Here, the proximity effects promote the precursor decomposition close to the substrate, leading to a gradual loop height reduction along the nanostructure.

Moreover, the number of scattered particles is also related to the substrate material: The more conductive the substrate is, the more effective the charge effects are, increasing the growth rate and influencing the final sizes. Thus, the employment of a conductive substrate can limit the charge effects for a better growth control.

Moreover, the values of step size and dwell time must be also adjusted: The former to control the density of the nucleation sites, and the latter to define the amount of deposited material during each deposition spot. It is worth noting also the role played by the local pressure of the gas precursor and the distance of the GIS from the substrate [59]; both influence the amount of the material that will be deposited.

Focused electron beam induced deposition is a technique very close to FIBID, but employs a high energy electron beam generated through a scanning electron microscope.

The growth mechanisms and the related properties are widely explored in literature [36][54][60][61]. We just remind that the most important difference between FIBID/FEBID growth of nanostructures consists of the achievable size and composition. In particular, FEBID allows for further reduction of the dimension of the fabricated nanostructures because of the smaller electron size, as compared to ions. Moreover, while the ion beam causes ion implantation that affects the final composition of the fabricated structures.

2.3. FIB under Cryogenic Conditions

A recent upgrade concerns FIB processing under cryogenic conditions, which cause the condensation of the precursor material on the substrate. Cryo-FIBID processes were realized and studied using tungsten [62] and platinum-based [63] precursors. The cryogenic temperatures can help to retain the microstructures of sensitive materials when performing milling treatments for electron microscopy [64]. For FIB induced deposition, the low process temperatures cause an ultrafast growth and, at the same time, reduce the proximity effects and the ion implantations [65] improving material composition [63].

3. Material Features of Nanostructure FIB Processing

Composition Assessment

A fundamental feature that so far hindered the widespread use of FIB processing in nanophotonics is the complex material composition of the fabricated nanostructures. FIB processing results in a low purity level [66], caused by the interaction between the ion beam with the substrate, because of the ion implantations and sputtered atoms redeposition. The low material purity is correlated with the incomplete dissociation of the gas precursor molecules, which leaves residual percentages of carbon and oxygen in the deposit. In addition, it is worth considering the contamination coming from the volatile residual species like CO and CO₂ present in the vacuum chamber, which contribute to the high carbon percentage, always recorded by the composition studies of the patterns/structures. The process parameters can also have a role in controlling gallium implantation, sputtered atom redeposition, and carbon percentage [67]. The presence of impurities might constitute a limitation on the functionality of the structures with respect to plasmonic applications, which require pure metallic surfaces. At the same time, the implantation of sputtered atoms and beam ions can introduce absorption losses in the optical response of otherwise transparent materials. Moreover, robust numerical and analytical modeling to understand and predict the structure optical behavior should rely on handbook-level or well-defined dispersions for the employed materials. Ideally, local optical investigation should be performed directly on FIB nanostructures to access the actual material dispersion, but this represents a challenging experimental issue, especially for chiral objects.

The compositional analysis of nanostructures manufactured by FIB processing (both milling and deposition) is usually performed by Energy Dispersive X-Ray Spectroscopy (EDS), transmission and scanning transmission electron microscopy (TEM and STEM respectively), Raman spectroscopy, Fourier Transform Infrared (FTIR) Spectroscopy, Auger electron spectroscopy (AES), and FIB cross section preparation [36].

During the milling process, the impurities introduced by the Ga⁺ implantations and re-deposition of the sputtered atoms can alter the fabricated nanostructure damaging the substrate [30]. Gallium implantation is detrimental in dielectric structures, increasing the absorption losses. This is the case of the 3D chiral photonic silicon platforms fabricated on sapphire (SOS) [68], shown in Figure 2a. Here, the STEM images, performed after the fabrication, demonstrated the presence of gallium implanted on a layer of damaged silicon (d-Si), and amorphous silicon inclusions (c-Si) (Figure 2b). The platforms have shown optical transmission lower than 20%. In order to remove impurities after the FIB milling process, a thermal oxidation treatment, followed by annealing, was carried out. The STEM image taken after the treatment (Figure 2c) demonstrated that the damaged silicon layer was replaced by silicon oxide. This cleaning procedure allowed for the improvement of the transmission intensity up to 70%. Moreover, the method proved advantageous for the fabrication of pure 3D chiral dielectric metasurfaces, exhibiting circular polarization discrimination in transmission in the visible range.

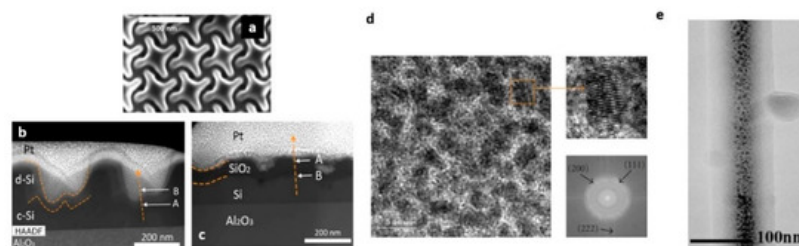


Figure 2. (a) Top view of FIB-milled 3D chiral photonic silicon nanostructures on a single crystal silicon film on sapphire. The period of the nanostructures was set to 370 nm. (b,c) Scanning transmission electron microscopy (STEM) cross-section images of the nanostructures before and after the annealing. A previous coating of a layer of platinum deposited in two stages has been applied as a protective layer. The STEM image taken before the annealing (b) shows: The presence of gallium implanted on the layer of damaged silicon (d-Si in the image) above the surface of the nanostructure, amorphous silicon inclusions (c-Si in the image), and the deposited protective platinum layer. The STEM image taken after the annealing shows that the d-Si is removed and a layer of silicon oxide is formed. Reproduced with permission from [68]. (d) HRTEM images of deposited Pt films grown on a copper grid show bright and dark regions associated to amorphous C region of carbon matrix and Pt grains, respectively. The inset shows the magnification of a Pt grain in order to observe the atomic planes, while the image below represents the diffraction spots of the Pt grains that correspond to the (200), (111), (222), and (202) atomic planes of fcc. Reproduced with permission from [69]. (e) TEM of an amorphous diamond like carbon (DLC) pillar. One can see the dark contrast of nanograins from the gallium core, while the bright part is the thick carbon shell, classified as diamond like carbon. Reproduced with permission from [70].

FIBID technology relies on a huge variety of available precursors, and consequently, materials that can be deposited. Organometallic precursors containing Pt, Au, Cu, and W have been originally developed for creating electric contacts and for mask repair. Nowadays, precursors of the noble metals, like gold or platinum, can be employed for plasmonic applications [74], while W precursors can serve for studies on superconductivity in FIBID nanostructures [57]. Precursors of magnetic materials (like cobalt) are of great interest for the fabrication of nanosensors, nanodevices, and for fundamental studies on nanomagnetism [56]. Many FIBID precursors have been also developed for carbon [72], which can be deposited in different forms, depending on growth conditions (39) (amorphous carbon, graphite, diamond, and diamond like carbon (DLC)) [73]. SiO₂ precursors for FIBID, like tetraethyl orthosilicate (SiC₈H₂₀O₄), have been used to deposit oxide films which displayed superior insulating properties and with low contamination [74].

Detailed compositional studies have been carried out on microstructures and thin films from organometallic precursors of platinum, copper, and gold [75][76][77]. In these cases, it was found that the deposits consist of metal nanocrystals, uniformly embedded in a matrix of amorphous carbon, exhibiting mechanical stability and chemical protection. A HRTEM image of FIBID Pt film deposited on a Cu grid is shown in Figure 2d, where the observed dark/bright contrast confirms the distribution of Pt nanoparticles immersed in the amorphous carbon matrix. Crystalline atomic planes and their related diffraction spots have been resolved, demonstrating the crystalline nature of metal grains [69]. These results demonstrated to be similar for Pt-based nanowires studied in other works [66][78].

Another representative case of the complex material architecture achieved by FIBID is when the Ga⁺ beam is used in conjunction with the precursor of a low molecular weight compound. Such a behavior has been firstly observed for pillar fabricated with phenanthrene (C₁₄H₁₀) and other carbon gaseous precursors [67][72][79]. Because of the gallium scattering length of 20–30 nm into the solid carbon [80], Ga ions are implanted in the nanostructure core, while the carbon is mainly confined in the outer part of the nanostructure forming a C-based shell. Figure 2e shows the TEM image of a carbon pillar, where the dark central part corresponds to the Ga core located at the center of the pillar, and the external part represents the amorphous carbon shell [70].

As an example of the compositional complexity that can be attained by FIBID, Figure 3 shows how the same nano-helix shape, realized by using three different precursors, can have completely different material architectures [81][82]. In particular, (methylcyclopentadienyl)platinum(IV) has been used for Pt, phenanthrene (C₁₀H₁₀) for C, and TEOS (Si(OC₂H₅)₄) for SiO₂. The high magnification of High Angle Annular Dark-field (HAADF) STEM image (Figure 3b) of the Pt-based nano-helix (Figure 3a) revealed an amorphous carbon matrix in which platinum metallic incursions (with averaged size 5 nm) are uniformly embedded. The distribution of elements in volume percentage throughout the nano-helix section is: 50% platinum, 45% carbon, and 5% of implanted gallium (Figure 3b,c). It is worth noting that the Pt nanograins are placed close to each other, leading to an overall metallic behavior, as discussed below.

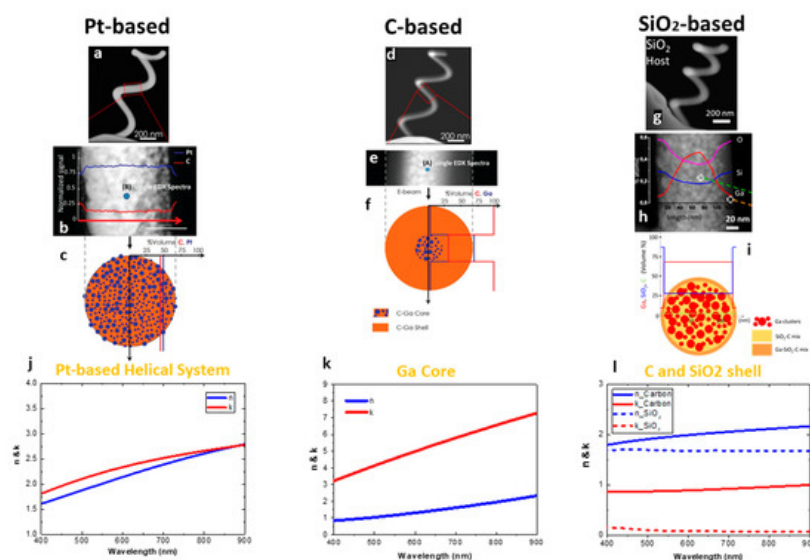


Figure 3. (a) STEM in HAADF (High Angle Annular Dark-field) image of a nanohelix realized with FIBID using Pt-precursor. (b) High-magnification STEM-HAADF image of a section of the Pt nanohelix. (c) Schematic view of the wire cross section which shows that the structure is composed by Pt nanograins embedded in an amorphous C matrix. The blue points correspond to Pt grains, while the amorphous carbon matrix is indicated in orange. (d) STEM in HAADF image of a nanohelix realized with FIBID using C-precursor. (e) High-magnification STEM-HAADF image of a section of the c nanohelix. (f) Scheme of the wire cross section of C nanowire made of Ga precipitates (diameter 1.5–4 nm) incorporated within a 30 nm core and an outer carbon shell. The blue spots indicate the gallium insert, while the orange indicates the carbon matrix. Reproduced with permission from [81]. Copyright © 2016, American Chemical Society. (g) STEM in HAADF

image of a nanohelix realized with FIBID using SiO₂-precursor. (h) High-magnification STEM-HAADF image of a section of the SiO₂ nanohelix. (i) Scheme of the wire cross section of SiO₂ nanowire, which displays Ga nanoparticles (with averaged diameter of 12 nm) and the outer SiO₂ shell. The red spots indicate the gallium insert, the yellow sites indicate the SiO₂ and carbon matrix, while the orange indicates the outer SiO₂ shell. Reproduced with permission from [82]. (j–l) Analytical dispersion values (n-blue line, k-red line) for the Pt-based (j), the core-shell C-based (k), and the SiO₂-based (l) nano-helices retrieved by FDTD simulations.

The HAADF-STEM image of a nano-helix (Figure 3d), grown by using phenanthrene as a carbon precursor, exhibits a core-shell profile with an inner core composed by gallium ions and an amorphous carbon shell, similarly to what was discussed before for carbon pillars and found in [76]. In particular, in the helix case, Ga nanoparticles concentrate inside a narrow core, with a volume percentage of 65%, whereas the thick outer shell is composed by 95% C and 5% Ga (Figure 3e,f). The SiO₂ nano-helix (Figure 3g) also exhibited a Ga-rich core (68% Ga/28% SiO₂/4% C) and a SiO₂-based shell (8% Ga/88% SiO₂/4% C). Even though the same growth parameters and structural features have been used, the Ga-core in the latter case is thicker than the former (Figure 3h,i). This happens because the Ga implantation in SiO₂ starts at the surface, given the large interaction between gallium ions and Si nuclei [83].

Starting from the structural composition observed by TEM/EDX analysis, a customized numerical model can be developed to retrieve the artificial material dispersions. The procedure was performed for the Pt-based structures (Figure 3j) and for both the core and shell of C and SiO₂ (Figure 3j,k, respectively) at the visible frequencies. The simulated effective refractive indexes (n) and absorption coefficients (k) underline the metallic behavior of the platinum wire, and of the gallium core, for both C and SiO₂ nano-helices in the visible range. On the other hand, the two shells exhibit a dielectric behavior with a lower absorption for the SiO₂-based shell.

The metal selection is fundamental for the generation of high-quality localized surface plasmon resonances (LSPRs) in nanostructures. Therefore, the material complexity of chiral FIBID/FEBID nanostructures can reduce their chiro-optical performances. In FEBID nanostructures, where gallium implantation does not occur, purification approaches of the deposited materials have been proposed just to remove the residual carbon content, with satisfactory results. These methods are: In situ substrate heating during the deposition process, post-treatment annealing in oxidizing atmospheres [84], electron irradiation or laser treatment of the structures [85], oxygen plasma [86], or ozone [87]. Another strategy, applied to both FIBID and FEBID nanostructures, consists of a post-process metal coating by means of thermal evaporation or sputter coating [59][88][89][90]. In this way, a metallic shell, thicker than the plasmonic skin depth, improves the plasmonic response from FIBID-based metal nanostructures [90].

Very few studies have been performed on FIBID structures, to our knowledge. Recently, a purification approach employing an oxygen flux during deposition was applied to planar platinum-based pads with 200 nm thickness [91]. Oxygen is suitable to form volatile species like CO and CO₂ and, thus, to reduce the carbon amount caused by the growth dynamics. Here, two different methods, both in situ and at room temperature, were applied: One is a post-deposition irradiation of a pad under O₂ flux; the second one consists of the simultaneous injection of oxygen and platinum precursors during the deposition. In both cases, the deposition occurred under the same growth conditions. Both experiments demonstrated a reduction of C/Pt ratio with a purity level close to bulk Pt. However, in the post deposition treatment, despite the efficient carbon removal, an increase of oxygen amount has been detected in the final nanostructure composition.

However the impurities are not necessarily harmful. As an example, it is possible to benefit from the effects of stress and strain caused by ion implantations on substrates during FIB milling to promote the fabrication of three-dimensional structures with broken symmetry [92]. Moreover, new frontiers in optics currently aim to research new plasmonic materials beyond noble metals [93]. For example, large chiroptical effects have been demonstrated as arising from the gallium plasmonic core in the Ga/SiO₂ core/shell nanohelices discussed above [82].

References

1. Liu, Y.; Zhang, X. Metamaterials: A new frontier of science and technology. *Chem. Soc. Rev.* 2011, 40, 2494–2507.
2. Liu, N.; Guo, H.; Fu, L.; Kaiser, S.; Schweizer, H.; Giessen, H. Three-dimensional photonic metamaterials at optical frequencies. *Nat. Mater.* 2008, 7, 31–37.
3. Ghasemi, R.; Leroux, X.; Degiron, A.; De Lustrac, A. *3D Optical Metamaterials*; Springer: Berlin, Germany, 2012; ISBN 9781441911506.
4. Di Fabrizio, E.; Schlücker, S.; Wenger, J.; Regmi, R.; Rigneault, H.; Calafiore, G.; West, M.; Cabrini, S.; Fleischer, M.; Van Hulst, N.F.; et al. Roadmap on biosensing and photonics with advanced nano-optical methods. *J. Opt.* 2016, 18.

5. Theories, C.; Problem, U. *The Origin of Chirality in the Molecules of Life*; Royal Society of Chemistry: Cambridge, UK, 2008; ISBN 9780854041565.
6. Blaschke, G.; Kraft, H.P.; Fickentscher, K.; Köhler, F. Chromatographic separation of racemic thalidomide and teratogenic activity of its enantiomers (author's transl). *Arzneimittelforschung* 1979, 29, 1640–1642.
7. Schäferling, M.; Dregely, D.; Hentschel, M.; Giessen, H. Tailoring enhanced optical chirality: Design principles for chiral plasmonic nanostructures. *Phys. Rev. X* 2012, 2, 1–9.
8. Collins, J.T.; Kuppe, C.; Hooper, D.C.; Sibilia, C.; Centini, M.; Valev, V.K. *Chirality and Chiroptical Effects in Metal Nanostructures: Fundamentals and Current Trends*. *Adv. Opt. Mater.* 2017, 5, 1–46.
9. Li, Z.; Mutlu, M.; Ozbay, E. Chiral metamaterials: From optical activity and negative refractive index to asymmetric transmission. *J. Opt.* 2013, 15.
10. Wang, Z.; Cheng, F.; Winsor, T.; Liu, Y. Optical chiral metamaterials: A review of the fundamentals, fabrication methods and applications. *Nanotechnology* 2016, 27, 1–20.
11. Hentschel, M.; Schäferling, M.; Duan, X.; Giessen, H.; Liu, N. Chiral plasmonics. *Sci. Adv.* 2017, 3, 1–13.
12. Urban, M.J.; Shen, C.; Kong, X.-T.; Zhu, C.; Govorov, A.O.; Wang, Q.; Hentschel, M.; Liu, N. Chiral Plasmonic Nanostructures Enabled by Bottom-Up Approaches. *Annu. Rev. Phys. Chem.* 2019, 70, 275–299.
13. Schäferling, M.; Yin, X.; Engheta, N.; Giessen, H. Helical Plasmonic Nanostructures as Prototypical Chiral Near-Field Sources. *ACS Photonics* 2014, 1, 530–537.
14. Hendry, E.; Carpy, T.; Johnston, J.; Popland, M.; Mikhaylovskiy, R.V.; Laphorn, A.J.; Kelly, S.M.; Barron, L.D.; Gadegaard, N.; Kadodwala, M. Ultrasensitive detection and characterization of biomolecules using superchiral fields. *Nat. Nanotechnol.* 2010, 5, 783–787.
15. Passaseo, A.; Esposito, M.; Cuscunà, M.; Tasco, V. Materials and 3D Designs of Helix Nanostructures for Chirality at Optical Frequencies. *Adv. Opt. Mater.* 2017, 5, 1–25.
16. Karst, J.; Cho, N.H.; Kim, H.; Lee, H.E.; Nam, K.T.; Giessen, H.; Hentschel, M. Chiral Scatterometry on Chemically Synthesized Single Plasmonic Nanoparticles. *ACS Nano* 2019, 13, 8659–8668.
17. Matsui, S. Focused-ion-beam deposition for 3-D nanostructure fabrication. *Nucl. Instrum. Methods Phys. Res. Sect. B Beam Interact. Mater. Atoms* 2007, 257, 758–764.
18. Reyntjens, S.; Puers, R. A review of focused ion beam applications in microsystem technology. *J. Micromech. Microeng.* 2001, 11, 287–300.
19. Reuss, R.H. Potential applications of focused ion beam technology for the semiconductor industry. *Nucl. Instrum. Methods Phys. Res. Sect. B Beam Interact. Mater. Atoms* 1985, 10–11, 515–521.
20. Nakamura, H.; Komano, H.; Ogasawara, M. Focused Ion Beam Assisted Etching of Quartz in XeF₂ without Transmittance Reduction for Phase Shifting Mask Repair. *Jpn. J. Appl. Phys.* 1992, 31, 4465–4467.
21. Stewart, D.K.; Doyle, A.F.; Casey, J.D., Jr. Focused ion beam deposition of new materials: Dielectric films for device modification and mask repair and tantalum films for x-ray mask repair. *Int. Soc. Opt. Photonics* 1995, 2437, 276–283.
22. Harriott, L.R.; Wagner, A.; Fritz, F. Integrated circuit repair using focused ion beam milling. *J. Vac. Sci. Technol. B Microelectron. Process. Phenom.* 1986, 4, 181–184.
23. Ishitani, T.; Yaguchi, T. Cross-sectional sample preparation by focused ion beam: A review of ion-sample interaction. *Microsc. Res. Tech.* 1996, 35, 320–333.
24. Langford, R.M.; Reeves, C.M.; Goodall, J.G.; Findlay, J.; Jeffree, C.E. Cantilever technique for the preparation of cross sections for transmission electron microscopy using a focused ion beam workstation. *J. Vac. Sci. Technol. B Microelectron. Nanom. Struct. Process. Meas. Phenom.* 2000, 18, 100–103.
25. Chen, Y.; Zhang, X. Focused ion beam technology and application in failure analysis. In *Proceedings of the 2010 11th International Conference on Electronic Packaging Technology & High Density Packaging*, Xi'an, China, 16–19 August 2010; pp. 957–960.
26. Olbrich, A.; Ebersberger, B.; Boit, C.; Niedermann, P.; Hänni, W.; Vancea, J.; Hoffmann, H. High aspect ratio all diamond tips formed by focused ion beam for conducting atomic force microscopy. *J. Vac. Sci. Technol. B Microelectron. Nanom. Struct. Process. Meas. Phenom.* 1999, 17, 1570–1574.
27. Krogmeier, J.R.; Dunn, R.C. Focused ion beam modification of atomic force microscopy tips for near-field scanning optical microscopy. *Appl. Phys. Lett.* 2001, 79, 4494–4496.
28. De Ridder, R.M.; Hopman, W.C.L.; Ay, F. Focused-ion-beam processing for photonics. In *Proceedings of the 2007 9th International Conference on Transparent Optical Networks*, Rome, Italy, 1–5 July 2007; Volume 2, pp. 212–215.

29. Kubena, R.L.; Ward, J.W.; Stratton, F.P.; Joyce, R.J.; Atkinson, G.M. A low magnification focused ion beam system with 8 nm spot size. *J. Vac. Sci. Technol. B Microelectron. Nanom. Struct. Process. Meas. Phenom.* 1991, 9, 3079–3083.
30. Editor, Z.M.W. *Nanostructures*; Springer: Berlin, Germany, 2013; ISBN 9783319028736.
31. Niessen, F.; Nancarrow, M.J.B. Computer-aided manufacturing and focused ion beam technology enable machining of complex micro- And nano-structures. *Nanotechnology* 2019, 30.
32. Keskinbora, K.; Grévent, C.; Eigenthaler, U.; Weigand, M.; Schütz, G. Rapid Prototyping of Fresnel Zone Plates via Direct Ga⁺ Ion Beam Lithography for High-Resolution X-ray Imaging. *ACS Nano* 2013, 7, 9788–9797.
33. Cai, J.; Zhu, Z.; Alkemade, P.F.A.; van Veldhoven, E.; Wang, Q.; Ge, H.; Rodrigues, S.P.; Cai, W.; Li, W.-D. 3D Volumetric Energy Deposition of Focused Helium Ion Beam Lithography: Visualization, Modeling, and Applications in Nanofabrication. *Adv. Mater. Interfaces* 2018, 5, 1800203.
34. Tseng, A.A. Recent Developments in Nanofabrication Using Ion Projection Lithography. *Small* 2005, 1, 594–608.
35. Joshi-Imre, A.; Bauerdick, S. Direct-Write Ion Beam Lithography. *J. Nanotechnol.* 2014, 2014, 1–26.
36. Utke, I.; Hoffmann, P.; Melngailis, J. Gas-assisted focused electron beam and ion beam processing and fabrication. *J. Vac. Sci. Technol. B Microelectron. Nanom. Struct.* 2008, 26, 1197.
37. Hahn, C.; Hajebifard, A.; Berini, P. Helium focused ion beam direct milling of plasmonic heptamer-arranged nanohole arrays. *Nanophotonics* 2020, 9, 393–399.
38. Chen, P.; Salemink, H.W.M.; Alkemade, P.F.A. Proximity effect in ion-beam-induced deposition of nanopillars. *J. Vac. Sci. Technol. B Microelectron. Nanom. Struct. Process. Meas. Phenom.* 2009, 27, 1838–1843.
39. Esposito, M.; Tasco, V.; Todisco, F.; Benedetti, A.; Sarvitto, D.; Passaseo, A. Three dimensional chiral metamaterial nanospirals in the visible range by vertically compensated focused ion beam induced-deposition. *Adv. Opt. Mater.* 2014, 2, 154–161.
40. van Kouwen, L. Chapter Seven—Introduction to focused ion beams, ion sources, and the nano-aperture ion source. In *Advances in Imaging and Electron Physics Including Proceedings CPO-10*; Hawkes, P.W., Hýtch, M.B.T.-A., Eds.; Elsevier: Amsterdam, The Netherlands, 2019; Volume 212, pp. 181–216. ISBN 1076-5670.
41. Bischoff, L. Alloy liquid metal ion sources and their application in mass separated focused ion beams. *Ultramicroscopy* 2005, 103, 59–66.
42. Bauerdick, S.; Bruchhaus, L.; Mazarov, P.; Nadzeyka, A.; Jede, R.; Fridmann, J.; Sanabia, J.E.; Gila, B.; Appleton, B.R. Multispecies focused ion beam lithography system and its applications. *J. Vac. Sci. Technol. B Nanotechnol. Microelectron. Mater. Process. Meas. Phenom.* 2013, 31, 06F404.
43. Tseng, A.A. Recent Developments in Nanofabrication Using Focused Ion Beams. *Small* 2005, 1, 924–939.
44. Melngailis, J. Focused ion beam technology and applications. *J. Vac. Sci. Technol. B Microelectron. Process. Phenom.* 1987, 5, 469–495.
45. Mackenzie, R.A.D.; Smith, G.D.W. Focused ion beam technology: A bibliography. *Nanotechnology* 1990, 1, 163–201.
46. Allen, F.I.; Velez, N.R.; Thayer, R.C.; Patel, N.H.; Jones, M.A.; Meyers, G.F.; Minor, A.M. Gallium, neon and helium focused ion beam milling of thin films demonstrated for polymeric materials: Study of implantation artifacts. *Nanoscale* 2019, 11, 1403–1409.
47. Abbas, A.N.; Liu, G.; Liu, B.; Zhang, L.; Liu, H.; Ohlberg, D.; Wu, W.; Zhou, C. Patterning, Characterization, and Chemical Sensing Applications of Graphene Nanoribbon Arrays Down to 5 nm Using Helium Ion Beam Lithography. *ACS Nano* 2014, 8, 1538–1546.
48. Yang, J.; Ferranti, D.C.; Stern, L.A.; Sanford, C.A.; Huang, J.; Ren, Z.; Qin, L.-C.; Hall, A.R. Rapid and precise scanning helium ion microscope milling of solid-state nanopores for biomolecule detection. *Nanotechnology* 2011, 22, 285310.
49. Marshall, M.M.; Yang, J.; Hall, A.R. Direct and Transmission Milling of Suspended Silicon Nitride Membranes With a Focused Helium Ion Beam. *Scanning* 2012, 34, 101–106.
50. Scholder, O.; Jefimovs, K.; Shorubalko, I.; Hafner, C.; Sennhauser, U.; Bona, G.-L. Helium focused ion beam fabricated plasmonic antennas with sub-5 nm gaps. *Nanotechnology* 2013, 24, 395301.
51. Burnett, T.L.; Kelley, R.; Winiarski, B.; Contreras, L.; Daly, M.; Gholinia, A.; Burke, M.G.; Withers, P.J. Large volume serial section tomography by Xe Plasma FIB dual beam microscopy. *Ultramicroscopy* 2016, 161, 119–129.
52. Dhawan, A.; Gerhold, M.; Madison, A.; Fowlkes, J.; Russell, P.E.; Vo-Dinh, T.; Leonard, D.N. Fabrication of nanodot plasmonic waveguide structures using FIB milling and electron beam-induced deposition. *Scanning* 2009, 31, 139–146.

53. Principe, M.; Consales, M.; Micco, A.; Crescitelli, A.; Castaldi, G.; Esposito, E.; La Ferrara, V.; Cutolo, A.; Galdi, V.; Cusano, A. Optical fiber meta-tips. *Light Sci. Appl.* 2017, 6, 16226.
54. Utke, I.; Michler, J.; Winkler, R.; Plank, H. Mechanical Properties of 3D Nanostructures Obtained by Focused Electron/Ion Beam-Induced Deposition: A Review. *Micromachines*. 2020, 11, 397.
55. Matsui, S.; Kaito, T.; Fujita, J.; Komuro, M.; Kanda, K.; Haruyama, Y. Three-dimensional nanostructure fabrication by focused-ion-beam chemical vapor deposition. *J. Vac. Sci. Technol. B Microelectron. Nanom. Struct.* 2000, 18, 3181.
56. Gazzadi, G.C.; Mulders, J.J.L.; Trompenaars, P.; Ghirri, A.; Rota, A.; Affronte, M.; Frabboni, S. Characterization of a new cobalt precursor for focused beam deposition of magnetic nanostructures. *Microelectron. Eng.* 2011, 88, 1955–1958.
57. Sadki, E.S.; Ooi, S.; Hirata, K. Focused-ion-beam-induced deposition of superconducting nanowires. *Appl. Phys. Lett.* 2004, 85, 6206–6208.
58. Fujita, J.; Ishida, M.; Sakamoto, T.; Ochiai, Y.; Kaito, T.; Matsui, S. Observation and characteristics of mechanical vibration in three-dimensional nanostructures and pillars grown by focused ion beam chemical vapor deposition. *J. Vac. Sci. Technol. B Microelectron. Nanom. Struct. Process. Meas. Phenom.* 2001, 19, 2834–2837.
59. Kusters, D.; De Hoogh, A.; Zeijlemaker, H.; Acar, H.; Rotenberg, N.; Kuipers, L. Core-Shell Plasmonic Nanohelices. *ACS Photonics* 2017, 4, 1858–1863.
60. Plank, H.; Winkler, R.; Schwalb, C.H.; Hütner, J.; Fowlkes, J.D.; Rack, P.D.; Utke, I.; Huth, M. Focused electron beam-based 3D nanoprinting for scanning probe microscopy: A review. *Micromachines* 2020, 11, 48.
61. Utke, I.; Gabureac, M.; Friedli, V.; Bernau, L.; Michler, J. In-situ monitoring of gas-assisted focused ion beam and focused electron beam induced processing. *J. Phys. Conf. Ser.* 2010, 241, 012072.
62. Córdoba, R.; Orús, P.; Strohauer, S.; Torres, T.E.; De Teresa, J.M. Ultra-fast direct growth of metallic micro- and nanostructures by focused ion beam irradiation. *Sci. Rep.* 2019, 9, 1–10.
63. Salvador-Porroche, A.; Sangiao, S.; Philipp, P.; Cea, P.; De Teresa, J.M. Optimization of pt-c deposits by cryo-fibid: Substantial growth rate increase and quasi-metallic behaviour. *Nanomaterials* 2020, 10, 1906.
64. Parmenter, C.D.J.; Fay, M.W.; Hartfield, C.; Eltaher, H.M. Making the practically impossible “Merely difficult”—Cryogenic FIB lift-out for “Damage free” soft matter imaging. *Microsc. Res. Tech.* 2016, 79, 298–303.
65. De Teresa, J.M.; Orús, P.; Córdoba, R.; Philipp, P. Comparison between focused electron/ion beam-induced deposition at room temperature and under cryogenic conditions. *Micromachines* 2019, 10.
66. Langford, R.M.; Wang, T.-X.; Ozkaya, D. Reducing the resistivity of electron and ion beam assisted deposited Pt. *Microelectron. Eng.* 2007, 84, 784–788.
67. Wanzenboeck, H.D.; Harasek, S.; Langfischer, H.; Bertagnolli, E. Deposition mechanism of oxide thin films manufactured by a focused energetic beam process. *Mater. Res. Soc. Symp. Proc.* 2002, 749, 305–310.
68. Rogov, O.Y.; Artemov, V.V.; Gorkunov, M.V.; Ezhov, A.A.; Khmelenin, D.N. FIB-fabricated complex-shaped 3D chiral photonic silicon nanostructures. *J. Microsc.* 2017, 268, 254–258.
69. De Teresa, J.M.; Córdoba, R.; Fernández-Pacheco, A.; Montero, O.; Strichovanec, P.; Ibarra, M.R. Origin of the Difference in the Resistivity of As-Grown Focused-Ion- and Focused-Electron-Beam-Induced Pt Nanodeposits. *J. Nanomater.* 2009, 2009, 936863.
70. Matsui, S. Focused-Ion-Beam Chemical-Vapor-Deposition (FIB-CVD) BT—Encyclopedia of Nanotechnology; Bhushan, B., Ed.; Springer: Dordrecht, The Netherlands, 2012; pp. 866–876. ISBN 978-90-481-9751-4.
71. Esposito, M.; Tasco, V.; Cuscunà, M.; Todisco, F.; Benedetti, A.; Tarantini, I.; De Giorgi, M.; Sanvitto, D.; Passaseo, A. Nanoscale 3D chiral plasmonic helices with circular dichroism at visible frequencies. *ACS Photonics* 2015, 2, 105–114.
72. Fujita, J.I.; Ishida, M.; Ichihashi, T.; Sakamoto, T.; Ochiai, Y.; Kaito, T.; Matsui, S. Structure and resonant characteristics of amorphous carbon pillars grown by focused-ion-beam-induced chemical vapor deposition. *Jpn. J. Appl. Phys. Part 1 Regul. Pap. Short Notes Rev. Pap.* 2002, 41, 4423–4426.
73. Kanda, K.; Yamada, N.; Okada, M.; Igaki, J.Y.; Kometani, R.; Matsui, S. Graphitization of thin films formed by focused-ion-beam chemical-vapor-deposition. *Diam. Relat. Mater.* 2009, 18, 490–492.
74. Lipp, S. Tetramethoxysilane as a precursor for focused ion beam and electron beam assisted insulator (SiOx) deposition. *J. Vac. Sci. Technol. B Microelectron. Nanom. Struct.* 1996, 14, 3920.
75. Tao, T. Focused ion beam induced deposition of platinum. *J. Vac. Sci. Technol. B Microelectron. Nanom. Struct.* 1990, 8, 1826.

76. Della Ratta, A.D.; Melngailis, J.; Thompson, C.V. Focused-ion beam induced deposition of copper. *J. Vac. Sci. Technol. B Microelectron. Nanom. Struct. Process. Meas. Phenom.* 1993, 11, 2195–2199.
77. Ro, J.S.; Thompson, C.V.; Melngailis, J. Microstructure of gold grown by ion-induced deposition. *Thin Solid Films* 1995, 258, 333–335.
78. Fernández-Pacheco, A.; De Teresa, J.M.; Córdoba, R.; Ibarra, M.R. Metal-insulator transition in Pt-C nanowires grown by focused-ion-beam- induced deposition. *Phys. Rev. B Condens. Matter Mater. Phys.* 2009, 79, 1–12.
79. Kometani, R.; Ishihara, S. Nanoelectromechanical device fabrications by 3-D nanotechnology using focused-ion beams. *Sci. Technol. Adv. Mater.* 2009, 10.
80. Kometani, R.; Ichihashi, T.; Kanda, K.; Suzuki, T.; Niihara, K.; Ishihara, S.; Kaito, T.; Matsui, S. Resistivity change of the diamondlike carbon, deposited by focused-ion-beam chemical vapor deposition, induced by the annealing treatment. *J. Vac. Sci. Technol. B Microelectron. Nanom. Struct. Process. Meas. Phenom.* 2008, 26, 2628–2631.
81. Esposito, M.; Tasco, V.; Todisco, F.; Cuscunà, M.; Benedetti, A.; Scuderi, M.; Nicotra, G.; Passaseo, A. Programmable Extreme Chirality in the Visible by Helix-Shaped Metamaterial Platform. *Nano Lett.* 2016, 16, 5823–5828.
82. Cuscuna, M.; Manoccio, M.; Esposito, M.; Scuderi, M. Materials Horizons polarization handling. *Mater. Horiz.* 2020.
83. Gnaser, H.; Brodyanski, A.; Reuscher, B. Focused ion beam implantation of Ga in Si and Ge: Fluence-dependent retention and surface morphology. *Surf. Interface Anal.* 2008, 40, 1415–1422.
84. Elbadawi, C.; Toth, M.; Lobo, C.J. Pure Platinum Nanostructures Grown by Electron Beam Induced Deposition. *ACS Appl. Mater. Interfaces* 2013, 5, 9372–9376.
85. Stanford, M.G.; Lewis, B.B.; Noh, J.H.; Fowlkes, J.D.; Rack, P.D. Inert Gas Enhanced Laser-Assisted Purification of Platinum Electron-Beam-Induced Deposits. *ACS Appl. Mater. Interfaces* 2015, 7, 19579–19588.
86. Haverkamp, C.; Höflich, K.; Jäckle, S.; Manzoni, A.; Christiansen, S. Plasmonic gold helices for the visible range fabricated by oxygen plasma purification of electron beam induced deposits. *Nanotechnology* 2017, 28.
87. Höflich, K.; Yang, R.B.; Berger, A.; Leuchs, G.; Christiansen, S. The direct writing of plasmonic gold nanostructures by electron-beam- induced deposition. *Adv. Mater.* 2011, 23, 2657–2661.
88. Wang, M.; Salut, R.; Lu, H.; Suarez, M.A.; Martin, N.; Grosjean, T. Subwavelength polarization optics via individual and coupled helical traveling-wave nanoantennas. *Light Sci. Appl.* 2019, 8.
89. Wozniak, P.; De Leon, I.; Hoich, K.; Haverkamp, C.; Christiansen, S.; Leuchs, G.; Banzer, P. Chiroptical response of a single plasmonic nanohelix. *Opt. Express* 2018, 26, 1513–1515.
90. Höflich, K.; Feichtner, T.; Hansjürgen, E.; Haverkamp, C.; Kollmann, H.; Lienau, C.; Silies, M. Resonant behavior of a single plasmonic helix. *Optica* 2019, 6, 1098.
91. Perez-Roldan, M.J.; Mulders, J.J.L.; Trompenaars, P.H.F. Oxygen-assisted purification of platinum structures deposited by ion and electron beam induced processes. *J. Phys. D. Appl. Phys.* 2017, 50.
92. Chen, Y.; Gao, J.; Yang, X. Chiral Metamaterials of Plasmonic Slanted Nanoapertures with Symmetry Breaking. *Nano Lett.* 2018, 18, 520–527.
93. Gutiérrez, Y.; Brown, A.S.; Moreno, F.; Losurdo, M. Plasmonics beyond noble metals: Exploiting phase and compositional changes for manipulating plasmonic performance. *J. Appl. Phys.* 2020, 128, 80901.